

Three-Dimensional FDTD Modeling of a Ground-Penetrating Radar

Levent Gürel, *Senior Member, IEEE*, and Uğur Oğuz

Abstract—The finite-difference time-domain (FDTD) method is used to simulate three-dimensional (3-D) geometries of realistic ground-penetrating radar (GPR) scenarios. The radar unit is modeled with two transmitters and a receiver in order to cancel the direct signals emitted by the two transmitters at the receiver. The transmitting and receiving antennas are allowed to have arbitrary polarizations. Single or multiple dielectric and conducting buried targets are simulated. The buried objects are modeled as rectangular prisms and cylindrical disks. Perfectly-matched layer absorbing boundary conditions are adapted and used to terminate the FDTD computational domain, which contains a layered medium due to the ground–air interface.

Index Terms—Finite-difference time-domain method (FDTD), ground-penetrating radar (GPR), perfectly matched layer, sub-surface scattering.

I. INTRODUCTION

THE APPARENT widespread interest in ground-penetrating radar (GPR) systems [1]–[3] have also created the need for a better understanding of subsurface-scattering mechanisms. Numerical modeling and simulation of GPR systems have been recognized as the preferred means for obtaining this understanding. A variety of differential equation and integral equation-based numerical modeling techniques have been developed for this purpose. Among these techniques, the finite difference time domain (FDTD) method [4] has been distinctively popular [5]–[13] due to its versatility in solving problems involving arbitrarily complicated inhomogeneities. In this paper, realistic three-dimensional (3-D) GPR scenarios are simulated using the FDTD method and the perfectly-matched layer (PML) [14]–[19] absorbing boundary conditions.

The geometry of the simulated problem is shown in Fig. 1. The ground–air interface lies at a constant- z plane in the computational domain. The PML regions surrounding the FDTD computational domain, are designed in a layered manner in order to match both the ground and air regions and the interface between them. Some of the details of this PML implementation are given in the Appendix. The air is modeled as vacuum (free space), and the ground is modeled as a homogeneous dielectric medium with arbitrary permittivity. We have also modeled lossy and inhomogeneous grounds, as reported elsewhere [20]. Buried scatterers of arbitrary quantity, shapes, locations, permittivities, permeabilities, and conductivities can be modeled.

The radar unit in Fig. 1, which contains the transmitting and receiving antennas, moves over the ground–air interface on a

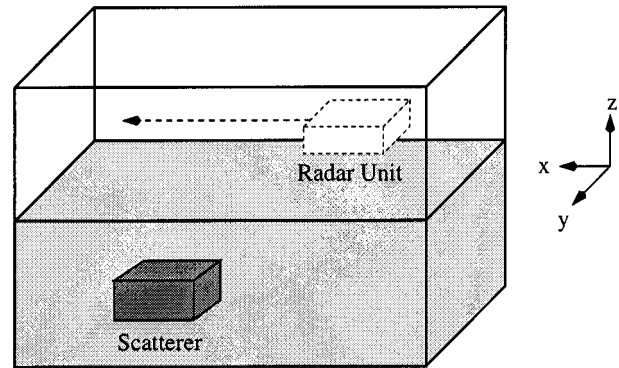


Fig. 1. Geometry of a half-space problem with a buried scatterer. A radar unit travels over the interface at a fixed elevation.

predetermined path. Section II will further elaborate on the details of the radar unit.

II. THE RADAR UNIT

A variety of GPR models, designed to achieve maximum scattered fields from the buried object in order to be able to detect the target, can be found in the literature [8]–[13]. In most cases, the radar unit consists of a transmitter T and a receiver R combined in a transmitter-receiver (TR) configuration, as depicted in Fig. 2(a) [6], [8]–[10]. Then, the total signal collected by the receiver contains not only the desired scattered signal S due to the buried object, but also the direct signal D (i.e., the incident field) due to the direct coupling from the transmitter to the receiver and the reflected signal G due to the reflection from the ground. Usually, the D signal is much larger than the desired S signal, rendering the detection of the S signal (and thus the buried object) difficult or impossible in the total received signal ($D + G + S$), which is dominated by the D signal. Some of the special techniques that can be employed to solve this problem are as follows.

- 1) The $D + G$ signal can be obtained, either computationally or through measurement, in the absence of the buried object(s). This signal can be subtracted from the total received signal to obtain the S signal [6], [8], [9].
- 2) In order to substantially weaken the D signal, the transmitter and the receiver can be isolated using conductive and/or absorbing shields [10], [13].
- 3) Using short pulses with high frequency contents, the D , G , and S signals can be separated in time in the total received signal. Then, the D or $D + G$ signal can be eliminated by windowing them out in time.

Manuscript received December 13, 1999; revised March 9, 2000.

The authors are with the Department of Electrical and Electronics Engineering, Bilkent University, Ankara, Turkey (e-mail: lgurel@ee.bilkent.edu.tr).

Publisher Item Identifier S 0196-2892(00)05910-6.

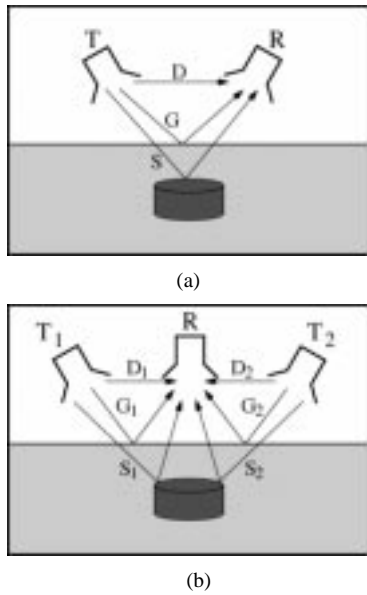


Fig. 2. (a) Transmitter-receiver (TR) and (b) transmitter-receiver-transmitter (TRT) configurations of the radar unit and the definition of the direct (D , D_1 , and D_2), reflected (G , G_1 , and G_2), and scattered (S , S_1 , and S_2) signals.

- 4) As an alternative to the time windowing, if the D and S signals can be separated in time using short pulses, then the total received signal can be multiplied by a scaling function that grows exponentially in time. This way, the S signal can be magnified to a level that allows comfortable detection even in the presence of the D signal.

In this work, radar units, each consisting of two transmitters and a receiver, are modeled in transmitter-receiver-transmitter (TRT) configurations [11] as shown in Fig. 2(b). The receiver R is located exactly in the middle of two identical transmitters (T_1 and T_2), 180° out of phase. In this configuration, the two direct signals D_1 and D_2 cancel each other at the receiver. Indeed, D_1 and D_2 cancel each other everywhere on a symmetry plane that is equidistant to the two transmitters. Similarly, the two reflected signals G_1 and G_2 also cancel out on the same symmetry plane and, in particular, at the receiver, if the ground is homogeneous and the ground-air interface is uniform. In that case, the total received signal becomes $S_1 + S_2$, which is solely due to the buried object. The inhomogeneities in the ground and on the ground-air interface contribute to the total received signal with their own small signals, which can be considered as noise on the desired $S_1 + S_2$ signal. Irrespective of the properties of the ground, the main advantage of the TRT configuration is the cancellation of the otherwise huge direct signal, which leads to the detection of the buried object. There are practical issues that would prevent the total cancellation of the D or G signals such as height variations or mismatches between antennas. However, even under those circumstances, most of the direct and ground signals would still cancel out at the receiver, which would still make the TRT configuration beneficial.

Section III presents the simulation results obtained with four GPR models, whose top views are shown in Fig. 3. The four TRT configurations in Fig. 3(a)–(d) are referred to as GPR1, GPR2, GPR3, and GPR4, respectively, and they differ from each

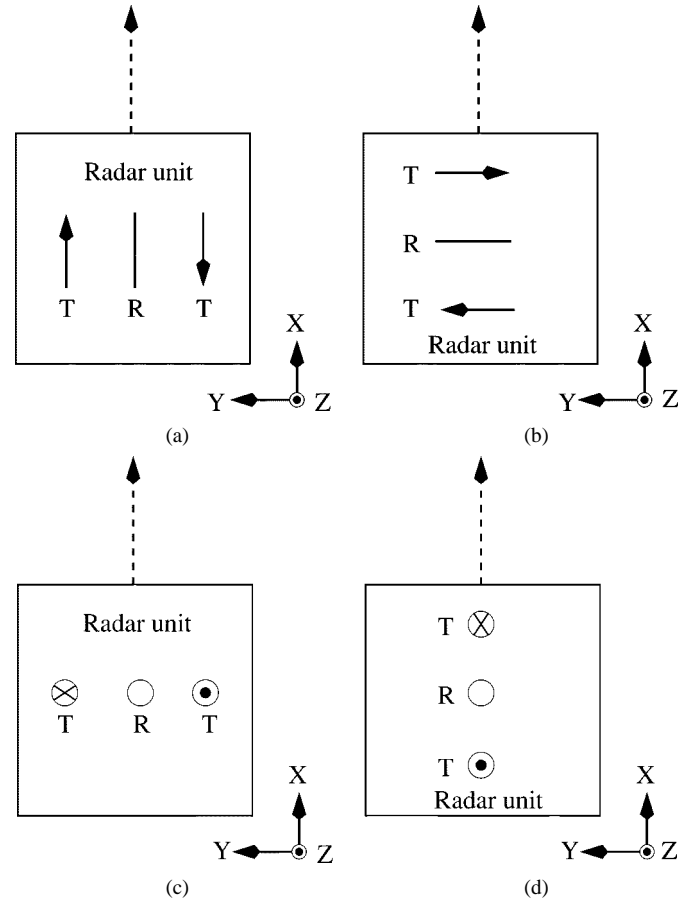


Fig. 3. GPR models used in this work. (a) GPR1: three x -polarized antennas aligned in the y direction. (b) GPR2: three y -polarized antennas aligned in the x direction. (c) GPR3: three z -polarized antennas aligned in the y direction. (d) GPR4: three z -polarized antennas aligned in the x direction.

other in the polarization and alignment of the three antennas. The transmitter antennas are selected as small dipoles, each of which is modeled by a single Yee cube of constant current density in its volume. The time variation of the current source is given by

$$J(t) = \frac{1}{\Delta^3} \left[4 \left(\frac{t}{\tau} \right)^3 - \left(\frac{t}{\tau} \right)^4 \right] e^{-\frac{t}{\tau}} \quad (1)$$

where

$$\tau = 1/(4\pi f_0) \quad (2)$$

f_0 is the center frequency of the pulse and $\Delta = \Delta x = \Delta y = \Delta z$ is the sampling interval in space.

The receiver is also modeled as a small dipole that samples and stores the values of the x , y , or z component of the electric field, depending on the choice of polarization. Thus, discrete values

$$E^{i,j,k,n} = E(i\Delta x, j\Delta y, k\Delta z, n\Delta t) \quad (3)$$

of the electric-field function $E(x, y, z, t)$ are obtained at the receiver. When the radar unit is stationary and the receiver collects data at a point (x_0, y_0, z_0) in space for successive instants

of time, this is called an A-scan, and the resulting data is denoted as

$$E^n = E(x_0, y_0, z_0, n\Delta t). \quad (4)$$

A B-scan is obtained by performing repeated A-scan measurements at discrete points on a linear path. For example, if the radar unit moves in the x direction, the collected B-scan data is denoted as

$$E^{i,n} = E(i\Delta x, y_0, z_0, n\Delta t). \quad (5)$$

Similarly

$$E^{i,j,n} = E(i\Delta x, j\Delta y, z_0, n\Delta t) \quad (6)$$

denotes the data collected on a rectangular grid of discrete points on a constant z plane. This measurement is called a C-scan and can be considered as combining several B-scans.

III. SIMULATION RESULTS

In this section, the four GPR models introduced in Section II are used to simulate several scenarios. In all of these simulations, the center frequency of the excitation is selected to be $f_0 = 1$ GHz for the pulse in (1). Sampling intervals in space and time are selected as $\Delta = 2.5$ mm, and $\Delta t = 4.5$ ps, respectively, which satisfies the Courant stability condition. The transmitting and receiving antennas of the radar units shown in Fig. 3 are separated by two cells (5 mm). The computer used in these simulations was a Digital AlphaServer 4100.

A. Conducting Prism

The four GPR models are first tested on a simple scenario. A perfectly conducting prism of $21 \times 16 \times 21$ cells ($5.25 \times 5.25 \times 4$ cm³) is located five cells (1.25 cm) under the ground-air interface. The relative permittivity of the ground is selected as $\epsilon_{ground} = 2$. B-scan data is collected with each radar unit as it travels over the edge of the conducting prism ($y = 11\Delta$) at a fixed elevation of ten cells (2.5 cm) over the ground ($z = 10\Delta$) and stops every 2Δ to perform an A-scan measurement (i.e., $E^{i,n} = E(i\Delta x, 11\Delta y, 10\Delta z, n\Delta t)$ for $i = -40, \dots, -2, 0, 2, \dots, 40$ with the desired polarization. Each A-scan signal is normalized and individually plotted in Figs. 4(a)–(d) to present the B-scan results as a function of the position of the radar unit (vertical axis) and time (horizontal axis), which can also be regarded as the depth variable. For each radar unit, the maximum value of the electric field obtained in a single B-scan

$$E_{\max} = \max_i \max_n E^{i,n} \quad (7)$$

is given in the title of each figure as an indication of the strength of the plotted signal. The largest of the four E_{\max} values corresponding to the four GPR models is used to normalize all four B-scan plots (i.e., all A-scan signals). Each A-scan measurement of the aforementioned simulation was solved in an FDTD computational domain consisting of $75 \times 75 \times 60$ Yee cells for 500 time steps. Eight-cell-thick PML walls were used to terminate the problem space. The observed CPU time for each A-scan was approximately 700 s.

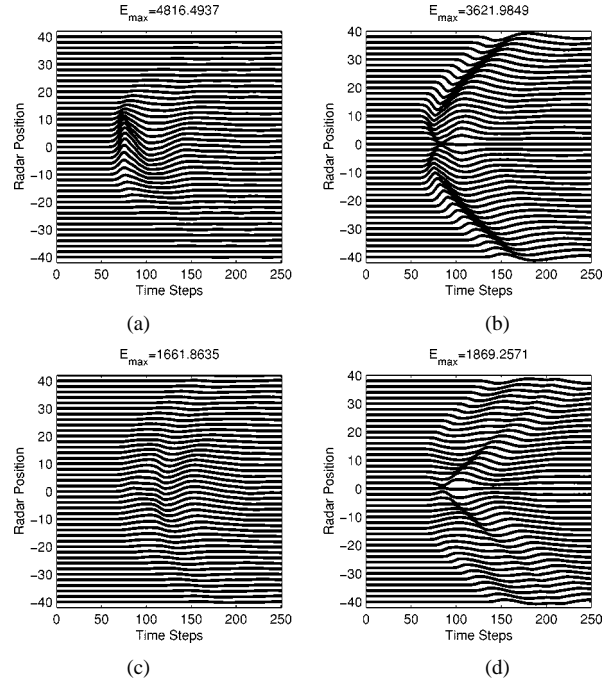


Fig. 4. Simulation results of a perfectly conducting rectangular prism buried five cells (1.25 cm) under the ground. The ground model has a relative permittivity of $\epsilon_{ground} = 2$. The simulations are carried out using (a) GPR1, (b) GPR2, (c) GPR3, and (d) GPR4. The radar unit travels on a linear path over the edge of the prism.

Comparison of Fig. 4(a)–(d) reveals that the responses of the four GPR models can be different even for the same scenario. For instance, for this case of radar unit traveling over the edge of the conducting prism, GPR1 collects electric fields with remarkably higher magnitudes compared to the other three configurations. Another difference among the four GPR models is the range of detection. GPR2 and GPR4 produce visible responses even when the radar unit is far from the buried object (i.e., near $x = -40\Delta$ and $x = 40\Delta$). On the other hand, GPR1 and GPR3 respond only when the radar unit is very close to the target, thus producing a localized response. The differences in the magnitude and the range of the four GPR models are due to the polarization of the antennas and can be used to facilitate the detection in a polarization-enriched GPR system.

Fig. 5(a)–(d) shows the results obtained with the four GPR models when the radar unit travels on a path that is almost centered with respect to the buried prism (i.e., on the $y = 0$ and $z = 10\Delta$ line). These results display significant differences compared to Figs. 4(a)–(d), namely, GPR1 and GPR3 receive remarkably weaker signals, whereas GPR2 and GPR4 receive considerably larger signals. The decrease in the fields received by GPR1 and GPR3 is due to the symmetry of the TRT configuration. When these two GPR models travel through a path that is centered with respect to the buried prism, the symmetry plane of the radar unit coincides with the symmetry plane of the buried object. That is, the scatterer also becomes symmetrical with respect to the receiver. Therefore, the two waves generated by the two transmitters and scattered by the prism cancel each other out at the receiver location. If the scatterer was modeled by an even number of cells in the y -direction, then there would be exactly zero fields at the receiver. Since the prism is 21 cells wide,

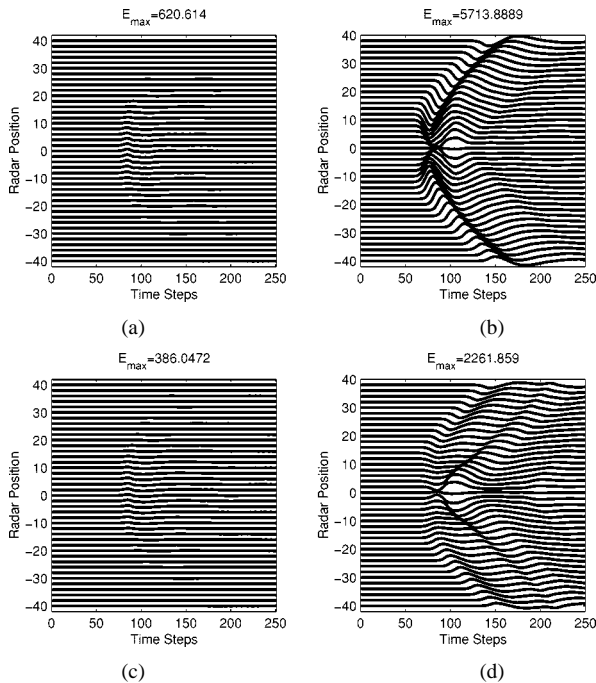


Fig. 5. Simulation results of a perfectly conducting rectangular prism buried five cells (1.25 cm) under the ground. The ground model has a relative permittivity of $\epsilon_{ground} = 2$. The simulations are carried out using (a) GPR1, (b) GPR2, (c) GPR3, and (d) GPR4. The radar unit travels on a linear path that is almost centered with respect to the buried object.

there is no exact symmetry in the problem. However, except for a one-cell-wide portion of it, the conducting prism is symmetrical with respect to the symmetry plane. Therefore, the signals reflecting from those symmetrical parts cancel each other and produce a weak scattered signal at the receiver.

The differences between Figs. 4 and 5 demonstrate that the choice of the path of measurement has a significant effect on the results. In order to further illustrate this effect and the symmetries in the problem, the radar units are moved on a two-dimensional grid, as opposed to a linear path. For each discrete radar position on the two-dimensional (2-D) grid, an A-scan measurement is performed, and the energy of the received A-scan signal is computed as

$$\text{Energy} = \sum_n |E^n|^2 \quad (8)$$

where E^n is defined in (4). Fig. 6(a) and (b) displays these energies on the 2-D grid obtained by two radar units consisting of x -polarized and z -polarized TRT dipoles, respectively. Since the radar units move in two directions, results obtained by the x -polarized configuration contain both GPR1 and GPR2 results, and the z -polarized configuration encompasses both GPR3 and GPR4 models. Constant- y and constant- x traces taken from the 2-D grid of Fig. 6 correspond to the energy plots of the waveforms obtained by GPR1 and GPR2, respectively. Similarly, Fig. 6(b) can be obtained by either GPR3 units moving in the x direction or GPR4 units moving in the y direction. For example, the energy plots of the waveforms given in Figs. 4(a) and 5(a) can be observed on paths $y = 10\Delta$ and $y = 0$ of Fig. 6(a), respectively.

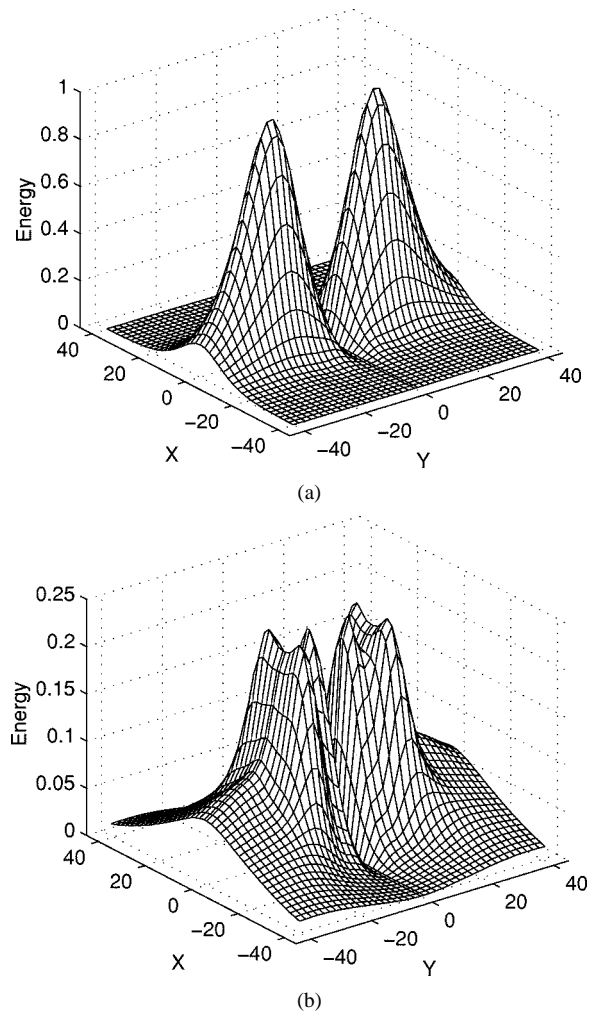


Fig. 6. Energy diagrams measured by (a) x -polarized and (b) z -polarized TRT radar units moving on a two-dimensional (2-D) grid. A perfectly conducting rectangular prism is buried five cells (1.25 cm) under the ground with a relative permittivity of $\epsilon_{ground} = 2$.

Fig. 6(a) and (b) depicts that GPR1 and GPR2 collect scattered energy that is four-times larger than GPR3 and GPR4. GPR2 and GPR4 collect the maximum energy on the symmetry plane ($x = 0$), where a minimum is encountered for GPR1 and GPR3 ($y = 0$). For this reason, GPR2 and GPR4 perform better in detecting the edges of the prism, whereas GPR1 and GPR3 respond to the whole mass of the buried target. The fact that GPR1 and GPR3 obtain weak signals on the $y = 0$ path, which coincides with the symmetry plane of the prism, does not constitute an insurmountable detection problem, since two clear energy peaks exist on the two sides of this path. A complete C-scan or even a few B-scans would easily detect these energy peaks.

Fig. 6(a) also shows that the energy levels observed by GPR1 and GPR2 from a distant scatterer are different in character. GPR2 receives a large amount of energy, while the radar unit moves away from the scatterer on a linear path, provided that the path itself is close to the buried target. For example, on the path $x = 0$ in Fig. 6(a), it is observed that the receiver of GPR2 collects a detectable amount of energy, while the radar unit moves 50 cells (12.5 cm) away from the center of the scatterer. However, if the path of GPR2 is not close to the scatterer

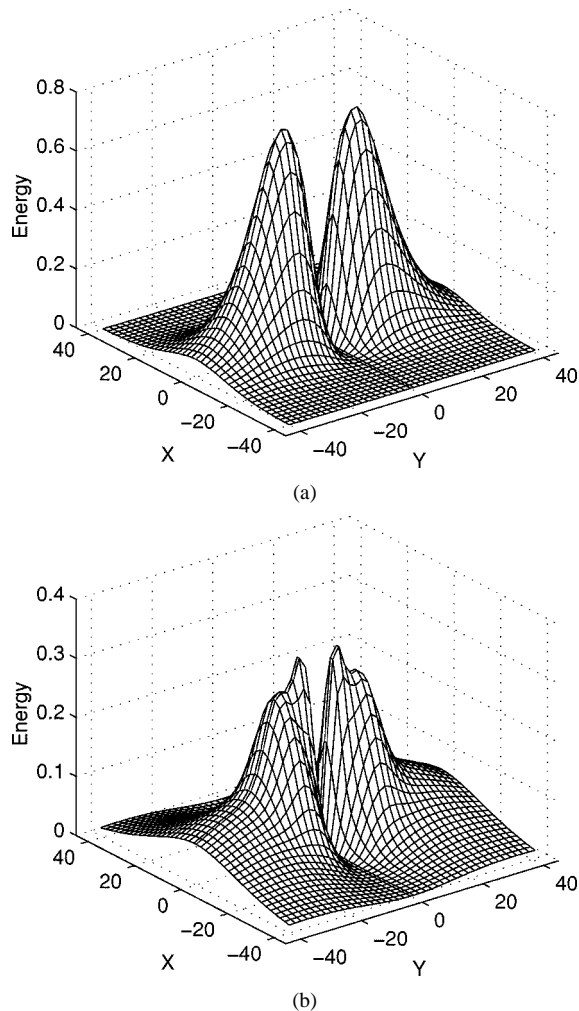


Fig. 7. Energy diagrams measured by (a) x -polarized and (b) z -polarized TRT radar units moving on a 2-D grid. A perfectly conducting disk is buried five cells (1.25 cm) under the ground with a relative permittivity of $\epsilon_{ground} = 2$.

(e.g., $x = -20\Delta$), the receiver collects an ignorable amount of energy everywhere on the path. On the other hand, GPR1 produces localized responses on a linear path, but these responses contain detectable levels of energy even if the path itself is away from the target (e.g., $y = -40\Delta$).

Each configuration with a different polarization has an advantage to it, and all of the results mentioned previously lead to the conclusion that multiple radar units with polarization diversity and multidimensional scans can facilitate the detection of the buried targets.

B. Conducting Disk

The 2-D scan of the previous section is repeated for a perfectly conducting disk with a radius of 10.5 cells (2.625 cm) and a height of 16 cells (4 cm) buried five cells (1.25 cm) under the ground. The relative permittivity of the ground is again selected as $\epsilon_{ground} = 2$, and the elevation of the GPR unit is again fixed as ten cells (2.5 cm). The results of the conducting disk given in Fig. 7 are similar to the results given in Fig. 6 for the prism. However, the four energy peaks due to the four corners of the prism in Fig. 6(b) are not present in Fig. 7(b). Moreover, due to the decrease in the volume and surface area of the scatterer, the

maximum energy levels observed with the horizontally-polarized radar units GPR1 and GPR2 are smaller in Fig. 7(a) compared to Fig. 6(a).

C. Dielectric Prism

The GPR is especially useful for the detection of dielectric objects. The contrast between the permittivities of the target and ground affects the resultant waveforms. In order to illustrate the effects of the relative permittivities of the ground and the target, a number of simulations with GPR1 and GPR2 have been performed, and the results are given in Fig. 8. In all of these simulations, a dielectric prism of size $21 \times 21 \times 16$ cells ($5.25 \times 5.25 \times 4\text{cm}^3$) is buried four cells (1 cm) under the ground-air interface, and the radar unit travels on the $y = -6\Delta$ and $z = 10\Delta$ linear path. The length of the horizontal axes of the plots in Fig. 8 are not chosen equal for the purpose of presenting all of the significant (nonzero) features of the data in the minimum amount of space.

In Fig. 8(a), the results of the simulations of GPR1 with a ground model of $\epsilon_{ground} = 2$ are given. The relative permittivities of the targets are 1, 4, 8, and 16. In this figure, the largest reflections are obtained from the dielectric prism with relative permittivity of 16, and the smallest reflection is obtained from the dielectric prism with relative permittivity of 1. Therefore, Fig. 8 demonstrates that as the contrast between the ground and the target increases, scattered fields observed at the receiver get larger in amplitude.

Each simulation result given in Fig. 8 displays two separate major reflections from the buried target, originated by the upper and lower faces of the dielectric prism. Fig. 8(a) demonstrates that if the permittivity of the target is larger than the permittivity of the ground, the second reflected signal is stronger than the first. That is, the reflection from the lower face of the target is larger than that from the upper face. However, if the ground is denser than the target, then the reflection from the upper face of the target is stronger. This is due to the larger reflections encountered while passing from a denser medium to a rarer one, mainly caused by total internal reflections. As the buried object becomes denser to make the permittivity contrast larger, stronger total internal reflections cause multiple reflections, which become visible in Fig. 8(a) as late-time effects following the two major reflections.

Fig. 8(b) and (c), where the relative permittivities of the ground models are selected as 4 and 8, respectively, lead to similar observations, namely, the maximum scattered fields are due to the largest target-background permittivity contrasts, and the dominant scattered waveforms from targets denser than the background are due to the reflections from the bottom of the target.

In order to investigate the effects of a different polarization, the simulations of Fig. 8(b) are repeated with a GPR2 radar unit traveling on the $y = 0$ and $z = 10\Delta$ linear path. Fig. 8(d) shows that, even though the features of the waveforms are quite different, the observations made previously concerning the dependence of the magnitude of the waveforms on the permittivity contrast and dominant latter reflections due to the targets denser than the background are also valid for GPR2.

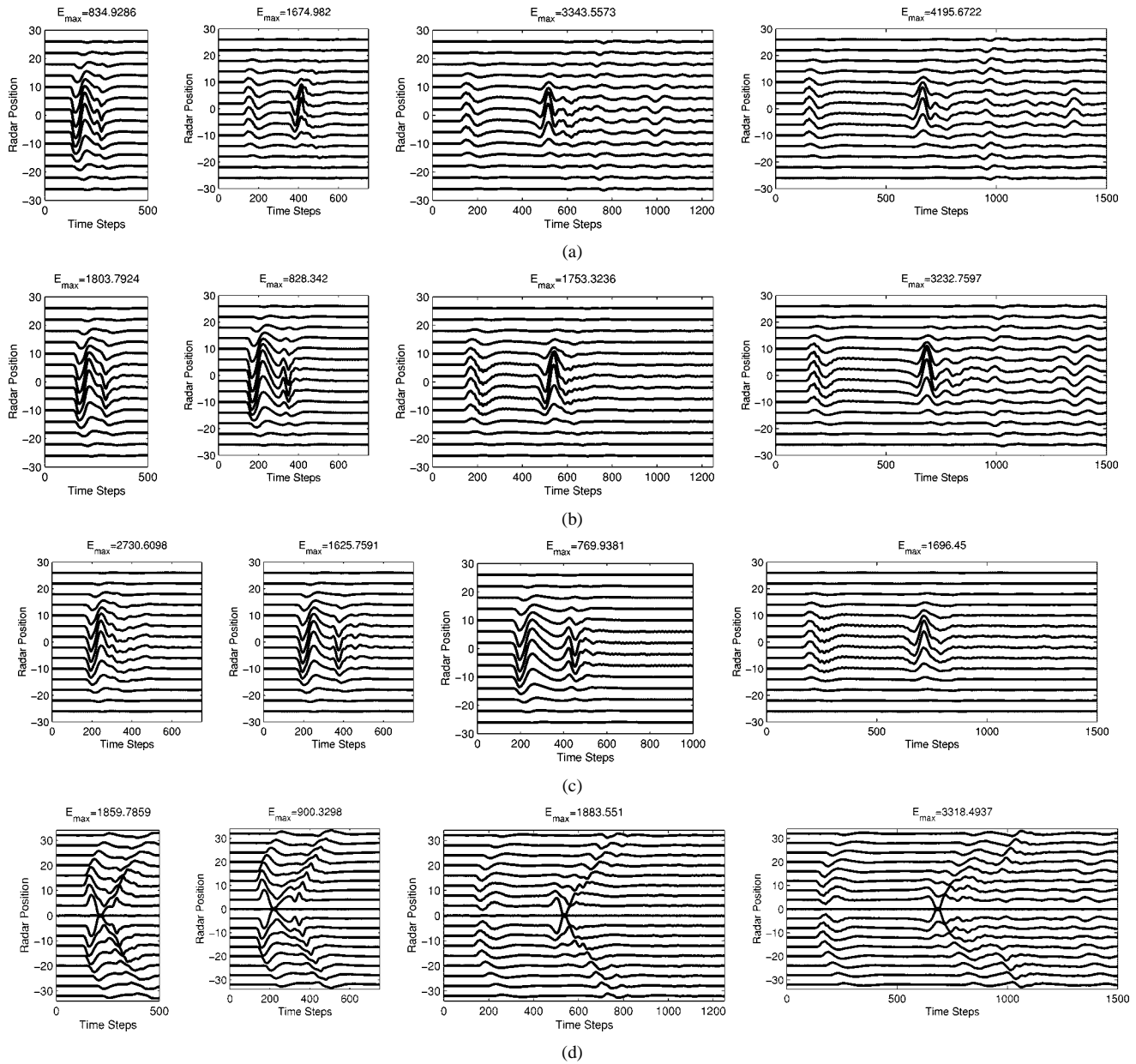


Fig. 8. B-scan results of a dielectric rectangular prism buried four cells (1 cm) under the ground. The results are obtained with (a) GPR1 and relative permittivities $\epsilon_{ground} = 2$ and $\epsilon_{target} = 1, 4, 8, 16$, (b) GPR1 and relative permittivities $\epsilon_{ground} = 4$ and $\epsilon_{target} = 1, 2, 8, 16$, (c) GPR1 and relative permittivities $\epsilon_{ground} = 8$ and $\epsilon_{target} = 1, 2, 4, 16$, and (d) GPR2 and relative permittivities $\epsilon_{ground} = 4$ and $\epsilon_{target} = 1, 2, 8, 16$. GPR1 travels on the $y = -6\Delta$ and $z = 10\Delta$ linear path, and GPR2 travels on a linear path that is almost centered ($y = 0$) with respect to the buried prism.

D. Multiple Targets

The previous sections demonstrate that GPR1 and GPR3 produce localized responses to nearby targets, whereas GPR2 and GPR4 respond to distant targets as well. The sensitivities of GPR1 and GPR3 to nearby targets can be beneficial for the detection of two closely buried objects. In order to investigate this situation, Fig. 9 presents the simulation results of a scenario, where two conducting prisms of $21 \times 21 \times 16$ cells ($5.25 \times 5.25 \times 4$ cm³) are buried five cells (1.25 cm) under the ground, separated by 20 cells (5 cm). In Fig. 9(a)–(d), the energies of the A-scan waveforms are evaluated according to (8) and are presented for GPR1–GPR4, in addition to the B-scan results. Fig. 9(a) shows that GPR1 produces signals that can be used for the detection of both objects. Fig. 9(c) shows that GPR3 can also

be used to some extent for the same purpose. Due to the symmetry properties explained in Section III-A, GPR2 and GPR4 produce zero signals as they pass near a symmetrical scatterer. Thus, one would have to seek the nulls or the minima of the energy in the GPR2 or GPR4 signals in order to detect a buried target. Fig. 9(b) and (d) displays nulls corresponding to the locations of the two objects. However, a third null corresponding to the symmetry plane of the combination of two objects complicates the detection process.

In order to investigate the performance of GPR1 on two closely buried targets of different materials, two other simulations are performed. In Fig. 10(a), the scattering results of a cavity and a dielectric object with relative permittivities $\epsilon_{cavity} = 1$ and $\epsilon_{object} = 8$, respectively, are given. The two

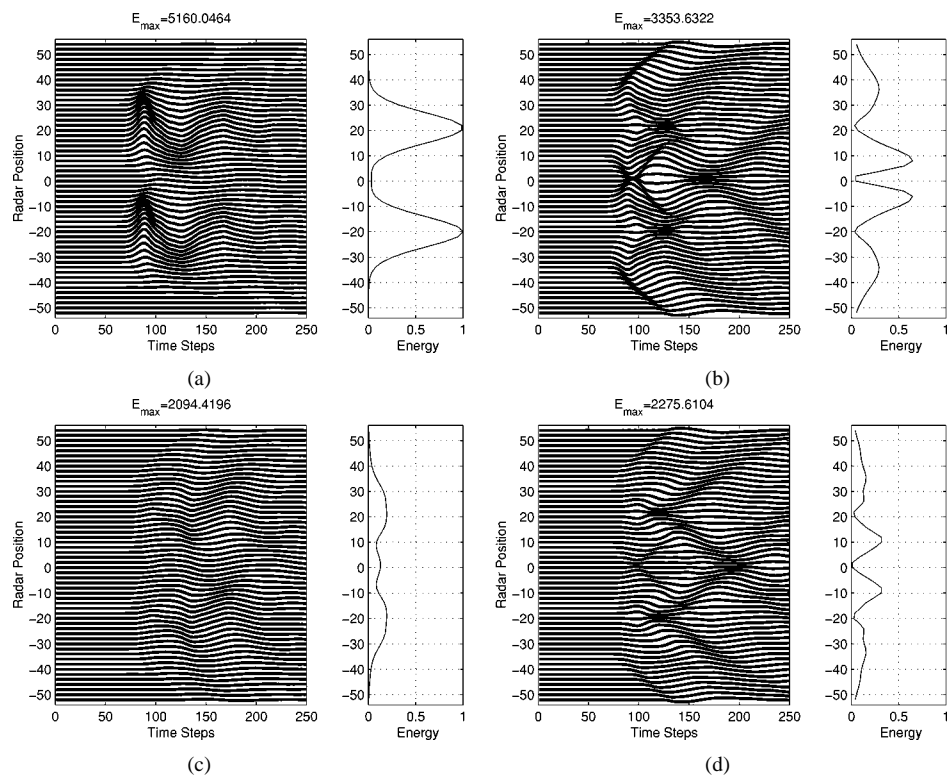


Fig. 9. Simulation results of two perfectly conducting rectangular prisms buried five cells (1.25 cm) under the ground and separated by 20 cells (5 cm). The ground has a relative permittivity of $\epsilon_{ground} = 4$. The simulations are carried out using (a) GPR1, (b) GPR2, (c) GPR3, and (d) GPR4. The path of the radar unit is offset by ten cells ($y = 10 \Delta$) from the symmetry plane ($y = 0$) of the buried objects. All B-scan results and all energy plots are normalized with respect to their maxima in (a).

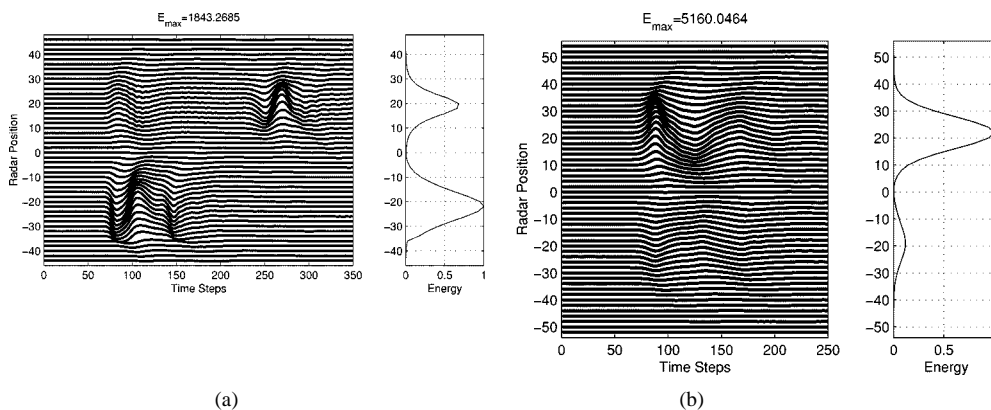


Fig. 10. Simulation results of two objects buried five cells (1.25 cm) under the ground and separated by 20 cells (5 cm). The results are obtained with GPR1. The ground has a relative permittivity of $\epsilon_{ground} = 4$. The objects are (a) a cavity (air bubble) with $\epsilon_{cavity} = 1$ and a dielectric object with $\epsilon_{object} = 8$, and (b) a cavity and a perfectly conducting object. All plots are independently normalized with respect to their own maxima.

targets are buried 20 cells (5 cm) apart and five cells (1.25 cm) under the ground, which has a relative permittivity of $\epsilon_{ground} = 4$. Fig. 10(a) depicts that GPR1 clearly detects the two objects, even though the energy peak produced by the cavity is much smaller than that of Fig. 9(a) for a conducting object, and the energy produced by the dielectric object is even smaller. It is also observed that the waveforms reflected from the cavity and the dielectric object have their own characteristics, as displayed in Fig. 8. In the second simulation, the dielectric prism is replaced by a conducting prism. Fig. 10(b) shows that the objects are again visible, although the cavity is a weaker scatterer compared to the conducting object. Note that the same

cavity is the stronger scatterer in Fig. 10(a) compared to the dielectric object.

IV. CONCLUDING REMARKS

The power and flexibility of the FDTD method are combined with the accuracy of the PML absorbing boundary conditions to simulate realistic GPR scenarios. Three-dimensional (3-D) geometries containing models of radar units, buried objects, and surrounding environments are simulated. In this paper, the radar unit is modeled as a TRT configuration, and the transmitting and

receiving dipole antennas are allowed to have different polarizations. The buried objects are modeled as rectangular prisms and cylindrical disks with arbitrary conductivities and permittivities. Multiple-target scenarios are also simulated.

Using the simulation results, the advantages and the disadvantages of both the TRT configuration and various polarizations of the dipole antennas are demonstrated. The major advantage of the TRT configuration is the total cancellation of the direct signals due to the direct coupling from the transmitters to the receiver and the partial cancellation of the reflected signals from the ground-air interface. Cancellation of these signals greatly facilitates the detection of the buried objects. GPR models with different antenna polarizations are shown to possess specific advantages, leading to the conclusion that polarization-enriched GPR systems should be preferred for better detection performance.

The simulations reported in this paper are carried out using a lossless homogeneous medium of arbitrary permittivity to model the ground. The performance of GPR systems with different configurations and polarizations over lossy and inhomogeneous ground models, including surface roughness, are also under study [20].

APPENDIX

PML ABSORBING BOUNDARY CONDITION FOR LAYERED MEDIA

The PML absorbing boundary condition is a nonphysical material boundary surrounding the computational domain. For a lossless and homogeneous medium, the matching conditions defined in the literature, e.g., [14]–[19], ensure a reflectionless transition to the PML region regardless of frequency and angle of incidence. However, subsurface-scattering problems involve layered media. For example, GPR simulations involve at least two layers (two half-spaces), one of which is the air (μ_0, ϵ_0), and the other of which is the ground (μ_0, ϵ_1). The ground medium can also be layered in itself.

Referring to the simple example depicted in Fig. 11, the matching condition for air is given by

$$\frac{\sigma_0}{\epsilon_0} = \frac{\sigma_0^*}{\mu_0} \quad (9)$$

while the matching condition for the top layer of the ground is given by

$$\frac{\sigma_1}{\epsilon_1} = \frac{\sigma_1^*}{\mu_0}. \quad (10)$$

At the air-ground interface (\overline{ab} in Fig. 11), the FDTD equations yield an effective permittivity of $(\epsilon_0 + \epsilon_1)/2$, to be used in the difference equations of tangential electric-field components. Thus, on the same constant- z plane of the PML region (\overline{bc} in Fig. 11), the conductivity values ($\sigma_{01}, \sigma_{01}^*$) should be matched to this effective permittivity value. The corresponding matching condition is given by

$$\frac{2\sigma_{01}}{\epsilon_0 + \epsilon_1} = \frac{\sigma_{01}^*}{\mu_0}. \quad (11)$$

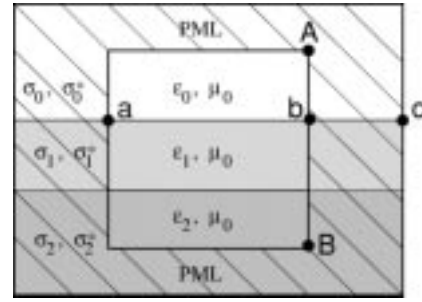


Fig. 11. Example of a stratified medium and the matching PML absorbing boundary conditions. Each portion of the PML is designed to absorb waves incident from a particular region of the computational domain.

In addition to the dielectric-PML matching conditions expressed in (9)–(11), yet another condition has to be satisfied. In order for the fields to be continuous on the two sides of the dielectric-PML interfaces (\overline{AB} in Fig. 11), Snell's law must predict the same angles of transmission at both the dielectric-dielectric (\overline{ab} in Fig. 11) and the PML-PML (\overline{bc} in Fig. 11) interfaces. More explicitly, Snell's law dictates at the dielectric-dielectric interface (\overline{ab}) that

$$\frac{\sin \theta_1}{\sin \theta_0} = \frac{\eta_1}{\eta_0} = \sqrt{\frac{\epsilon_0}{\epsilon_1}} \quad (12)$$

and at the PML-PML interface (\overline{bc}), that

$$\frac{\sin \theta_1}{\sin \theta_0} = \frac{\sqrt{\frac{\mu_0 + i \frac{\sigma_1^*}{\omega}}{\epsilon_1 + i \frac{\sigma_1^*}{\omega}}}}{\sqrt{\frac{\mu_0 + i \frac{\sigma_0^*}{\omega}}{\epsilon_0 + i \frac{\sigma_0^*}{\omega}}}} \quad (13)$$

where θ_0 is the angle of incidence of any arbitrary plane-wave component of the field in layer 0, and θ_1 is the corresponding angle of transmission in layer 1. Substituting σ_0^* and σ_1^* from (9) and (10) into (13), we obtain

$$\frac{\sin \theta_1}{\sin \theta_0} = \frac{\sqrt{\frac{\mu_0 + i \frac{\mu_0 \sigma_1}{\epsilon_1 \omega}}{\epsilon_1 + i \frac{\sigma_1^*}{\omega}}}}{\sqrt{\frac{\mu_0 + i \frac{\mu_0 \sigma_0}{\epsilon_0 \omega}}{\epsilon_0 + i \frac{\sigma_0^*}{\omega}}}}. \quad (14)$$

The aforementioned condition requires that the ratios in (12) and (14) be equal. This is satisfied if the electric conductivities σ_0 and σ_1 are selected such that

$$\frac{\sigma_0}{\epsilon_0} = \frac{\sigma_1}{\epsilon_1}. \quad (15)$$

In the presence of several layers, (15) is generalized as

$$\frac{\sigma_0}{\epsilon_0} = \frac{\sigma_1}{\epsilon_1} = \frac{\sigma_2}{\epsilon_2} = \dots = \frac{\sigma_n}{\epsilon_n}. \quad (16)$$

With the use of (16) together with (9)–(11) for each layer, the implementation of the PML absorbing boundary conditions for layered media becomes possible and, indeed, straightforward.

REFERENCES

- [1] D. J. Daniels, *Surface-Penetrating Radar*. London, U.K.: IEE, 1996.

- [2] *Proc. Detection and Remediation Technologies for Mines and Minelike Targets III*, A. C. Dubey, J. F. Harvey, and J. T. Broach, Eds., Orlando, FL, Apr. 1998.
- [3] *Proc. GPR'98, 7th Int. Conf. Ground-Penetrating Radar*, Univ. Kansas, Lawrence, KS, May 1998.
- [4] K. S. Yee, "Numerical solution of initial boundary value problems involving Maxwell's equations in isotropic media," *IEEE Trans. Antennas Propagat.*, vol. 14, pp. 302–307, May 1966.
- [5] M. Moghaddam, W. C. Chew, B. Anderson, E. J. Yannakakis, and Q. H. Liu, "Computation of transient electromagnetic waves in inhomogeneous media," *Radio Sci.*, vol. 26, pp. 265–273, Jan. 1991.
- [6] M. Moghaddam, E. J. Yannakakis, W. C. Chew, and C. Randall, "Modeling of the subsurface interface radar," *J. Electromagn. Waves Applicat.*, vol. 5, no. 1, pp. 17–39, 1991.
- [7] K. Demarest, R. Plumb, and Z. Huang, "FDTD modeling of scatterers in stratified media," *IEEE Trans. Antennas Propagat.*, vol. 43, Oct. 1995.
- [8] J. M. Bourgeois and G. S. Smith, "A fully three-dimensional simulation of a ground-penetrating radar: FDTD theory compared with experiment," *IEEE Trans. Geosci. Remote Sensing*, vol. 34, pp. 36–44, Jan. 1996.
- [9] U. Oğuz and L. Gürel, "Subsurface-scattering calculations via the 3D FDTD method employing PML ABC for layered media," in *1997 IEEE AP-S Int. Symp. URSI Radio Science Meeting*, Montréal, PQ, Canada, July 1997.
- [10] J. M. Bourgeois and G. S. Smith, "A complete electromagnetic simulation of the separated-aperture sensor for detecting buried land mines," *IEEE Trans. Antennas Propagat.*, vol. 46, pp. 1419–1426, Oct. 1998.
- [11] P. Luneau and G. Y. Delisle, "Underground target probing using FDTD," in *1996 IEEE AP-S Int. Symp. URSI Radio Science Meeting*, Baltimore, MD, July 1996, pp. 1664–1667.
- [12] F. L. Teixeira, W. C. Chew, M. Straka, and M. L. Oristaglio, "Finite-difference time-domain simulation of ground-penetrating radar on dispersive, inhomogeneous, and conductive soils," *IEEE Trans. Geosci. Remote Sensing*, vol. 36, pp. 1928–1937, Nov. 1998.
- [13] L. Gürel and U. Oğuz, "Employing PML absorbers in the design and simulation of ground penetrating radars," in *1999 IEEE AP-S Int. Symp. USNC/URSI National Radio Science Meeting*, Orlando, FL, July 1999, pp. 1890–1893.
- [14] J. P. Berenger, "A perfectly matched layer for the absorption of electromagnetic waves," *J. Comput. Phys.*, pp. 185–200, Oct. 1994.
- [15] W. C. Chew and W. H. Weedon, "A 3D perfectly matched medium from modified Maxwell's equations with stretched coordinates," *Microw. Opt. Technol. Lett.*, vol. 7, pp. 599–604, Sept. 1994.
- [16] D. S. Katz, E. T. Thiele, and A. Taflove, "Validation and extension to three dimensions of the Berenger PML absorbing boundary condition for FD-TD meshes," *IEEE Microwave Guided Wave Lett.*, vol. 4, no. 8, pp. 268–271, Aug. 1995.
- [17] J. B. Verdu, R. Gillard, K. Moustadir, and J. Citerne, "An extension of the PML technique to the FDTD analysis of multilayer planar circuits and antennas," *Microw. Opt. Technol. Lett.*, vol. 10, pp. 323–327, Dec. 1995.
- [18] J. Fang and Z. Wu, "Generalized perfectly matched layer for the absorption of propagating and evanescent waves in lossless and lossy media," *IEEE Trans. Microwave Theory Technol.*, vol. 44, pp. 2216–2222, Dec. 1996.

- [19] D. Johnson, C. Furse, and A. Tripp, "Application and optimization of the perfectly matched layer boundary condition for geophysical simulations," unpublished.
- [20] U. Oğuz and L. Gürel, private communication, "Simulations of ground-penetrating radars over lossy and heterogeneous grounds," unpublished.



Levent Gürel (S'87–M'92–SM'97) was born in Izmir, Turkey, in 1964. He received the B.Sc. degree from the Middle East Technical University (METU), Ankara, Turkey, in 1986, and the M.S. and Ph.D. degrees from the University of Illinois, Urbana (UIUC), in 1988 and 1991, respectively, all in electrical engineering.

He joined the Thomas J. Watson Research Center, IBM Corporation, Yorktown Heights, New York, in 1991, where he worked as a Research Staff Member on the electromagnetic compatibility (EMC) problems related to electronic packaging, the use of microwave processes in the manufacturing and testing of electronic circuits, and the development of fast solvers for interconnect modeling. He then became an Associate Professor with the Institute of Higher Education, Ankara, in 1993. Since 1994, he has been a Faculty Member, Department of Electrical and Electronics Engineering, Bilkent University, Ankara. He was a Visiting Associate Professor at the Center for Computational Electromagnetics (CCEM), UIUC, for one semester in 1997. His research interests include the development of fast algorithms for computational electromagnetics (CEM) and the application thereof to scattering and radiation problems involving large and complicated scatterers, antennas and radars, frequency-selective surfaces, and high-speed electronic circuits. He is also interested in the theoretical and computational aspects of electromagnetic compatibility and interference analyses. Ground penetrating radars and other subsurface scattering applications are also among his current research interests.

Dr. Gürel is currently serving as the Chairman of the AP/MTT/ED Chapters of the IEEE Turkey Section.



Uğur Oğuz was born in Ankara, Turkey, in 1973. He received the B.Sc. and M.Sc. degrees, both in electrical engineering, from Bilkent University, Ankara, Turkey, in 1994 and 1997, respectively.

From August 1997 to October 1998, he served in the Turkish Army as a database manager and system administrator. Since November 1998, he has been a Research Engineer with the Department of Electrical and Electronics Engineering, Bilkent University. His research interests include time-domain methods in computational electromagnetics and their applica-

tions to geophysical problems.